Draft version December 2, 2016
Preprint typeset using LaTeX style emulateapj v. 08/22/09

arXiv:1612.00022v1 [astro-ph.GA] 30 Nov 2016

RADIATION HYDRODYNAMIC SIMULATIONS OF DUST-DRIVEN WINDS

Dong Zhang[1] and Shane W. Davis[1]
Department of Astronomy, University of Virginia, Charlottesville, VA 22904, USA
Draft version December 2, 2016

ABSTRACT

We study dusty winds driven by radiation pressure in the atmosphere of a rapidly star-forming environment. We apply the variable Eddington tensor algorithm to re-examine the two-dimensional radiation hydrodynamic problem of a column of gas that is accelerated by a constant infrared radiation flux. In the absence of gravity, the system can be characterized by the initial optical depth of the gas. We perform several runs with different initial optical depth and resolution. We find that the gas spreads out along the vertical direction, as its mean velocity and velocity dispersion increase. In contrast to previous work using flux-limited diffusion algorithm, we find little evolution in the trapping factor. The momentum coupling between radiation and gas in the absence of gravity is similar to that with gravity. For Eddington ratio increasing with the height in the system, the momentum transfer from the radiation to the gas is not merely $\sim L/c$, but amplified by a factor of $1+\eta\tau_{\rm IR}$, where $\tau_{\rm IR}$ is the integrated infrared optical depth through the system, and $\eta\sim 0.5-0.9$, decreasing with the optical depth. We apply our results to the atmosphere of galaxies and conclude that radiation pressure may be an important mechanism for driving winds in rapidly star-forming galaxies and starbursts.

Subject headings: galaxies: ISM — hydrodynamics — ISM: jets and outflows — methods: numerical — radiative transfer

1. INTRODUCTION

Feedback processes play a crucial role in galaxy formation and evolution. In particular, radiation pressure from the continuum absorption and scattering of starlight on dust grains has been proposed as an important mechanism in driving supersonic turbulence in the interstellar medium (ISM), hampering gravitational collapse, and launching large-scale galactic winds in starbursts and rapidly star-forming galaxies. One-dimensional analytic models show that dusty winds can be driven by radiation pressure in rapidly star-forming environments, such as luminous infrared galaxies (LIRGs) and ultraluminous infrared galaxies (ULIRGs) (e.g., Thompson et al. 2005; Murray et al. 2005; Murray et al. 2011; Zhang & Thompson 2012).

However, the simplified galactic wind models contain some uncertainties. A key question that cannot be addressed by analytic models is how much momentum is coupled between radiation and dusty gas. In the single scattering limit, i.e., the system is optically thick to the UV photons, but optically thin to the re-radiated infrared (IR) emission from dust grains, all photons are absorbed and scattered once, the radiation transfers a momentum flux of L/c in the gas, where L is the luminosity of radiation source. However, it is uncertain how much momentum is transferred from radiation to gas if the system is optically thick to its own infrared emission. It has been argued that the rate of momentum deposition will never exceed a few of L/c (Krumholz & Matzner 2009), or it approaches $\tau_{\rm IR}L/c$, where $\tau_{\rm IR}\gg 1$ is the mean IR optical depth of the system (Thompson et al. 2005; Murray et al. 2010; Andrews & Thompson 2011; Thompson et al. 2015). In order to understand the dynamics of radiation-gas interaction, multidimensional radiation hydrodynamics simulations have been carried out recently.

Krumholz & Thompson (2012, hereafter KT12) used a 2-dimensional (2D) model to investigate the efficiency of momentum transfer from IR opticlaly thick ultraluminous infrared galaxies (ULIRGs) to a dusty atmosphere with a vertically stratified gravity. Using 2D grey flux-limited diffusion (FLD) approximation in the ORION code (Krumholz et al. 2007), KT12 showed that the radiation-gas interaction gives rise to radiative Rayleigh-Taylor instability (RTI), driving supersonic turbulence, and limiting momentum transfer from the radiation to the gas to $\sim L/c$. The radiation momentum deposition in the regime where is initially sub-Eddington for dust is not sufficient to driven an unbound wind, most of the gas is eventually settled in a turbulent steady state confined near the base of the system.

However, using a more sophisticated radiation hydrodynamics implementation of the variable Eddington tensor (VET) algorithm in the ATHENA code (Stone et al. 2008; Davis et al. 2012; Jiang et al. 2012), Davis et al.(2014, hereafter D14) revisited the results of KT12 with the same 2D and 3D setups. The VET algorithm is used to calculate the local Eddington tensor by solving the radiative transfer equation with the method of short characteristics (Davis et al. 2012). In contrast to KT12, D14 showed a stronger momentum coupling between radiation and dusty gas. Although the radiative RTI develops and limit the radiation-gas interaction, The gas can be heated and accelerated upward by radiation, and produce an unbound outflow even from an initially sub-Eddington system for dust. The significant difference between KT12 and D14 results from limitations in the diffusion-based FLD scheme. The FLD and VET schemes agree well in the dense gas with optical depth $\tau_{\rm IR}\gg 1$, but the FLD approximation becomes inaccurate in modeling the radiation field responds to structure in the gas distribution in the system of $\tau_{\rm IR}\lesssim$ few.

Electronic address: dz7g@virginia.edu

Rosdah & Teyssier (2015) simulated the same problem of KT12 and D14 using their new RAMSES-RT code with the M1 closure for the Eddington tensor. Their results are qualitatively closer to those obtained with the FLD rather than with the VET method. Like FLD, in the M1 closure algorithm the radiation force is ultimately insufficient to overcome the gravity, and the gas eventually settles down in an initially sub-Eddington system. On the other hand, more recently simulation based on the implicit Monte Carlo radiation transfer scheme is more consistent with D14 (Tsang & Milosavljević 2015). Among a variety of algorithms, including ray tracing from point sources, flux-limited diffusion, M1 closure and VET, VET has been demonstrated to have the most accurate methods for problems involving a diffuse radiation field.

Note that in the previous mentioned simulations of radiation-gas interaction, the size of the computational box is only about ~ 0.3 pc$\times$1.3 pc, with a resolution of $\Delta x \simeq 3.2\times10^{-4}$ pc, so that one can resolve the sound crossing timescale and the scale of gas turbulence. In order to investigate the efficiency of momentum coupling and wind propagation on a larger scale, Krumholz & Thompson (2013, hereafter KT13) assumed that a wind is initially launched at the base of the galactic atmosphere due to super-Eddington radiation forces or other mechanisms, and turned off the gravity to study the maximum velocity the gas can gain from radiation. Using also ORION and the FLD scheme, KT13 found that after wind acceleration begins, RTI forces the gas into a configuration that reduces the rate of momentum transfer from the radiation filed to the gas by a factor of $\sim 10-100$ compared to an estimate based on the optical depth at the base of the atmosphere, the momentum transfer to gas is only a few of $\sim L/c$, without significant amplification by radiation trapping. They concluded that radiation pressure on dust is unlikely to be able to drive winds and ejecta from star-forming clusters and galaxies. So far, no other simulations have been done for the wind-gas interaction problem. Given previous discrepancies, it is important to re-examine the results of KT13 using the VET method.

This paper is organized as follows. In Section 2 we briefly summarize the equations and the simulation setup. The initial conditions of the gas are given by the end states of the simulations from D14. In Section 3 we show our simulation with various parameters, and summarize our results. The astrophysical implications are discussed in Section 4. Conclusions are given in Section 5.

2. EQUATIONS AND SIMULATION SETUP

2.1. *Equations*

As in D14, we solve the equations of radiation hydrodynamics using ATHENA with the built-in radiation module (Davis et al. 2012; Jiang et al. 2012). The equations of mass, momentum, energy, radiation energy and radiation momentum conservation are

$$\frac{\partial\rho}{\partial t}+\nabla\cdot(\rho\mathbf{v})=0, \tag{1}$$

$$\frac{\partial(\rho\mathbf{v})}{\partial t}+\nabla\cdot(\rho\mathbf{v}\mathbf{v}+\mathsf{P})=\rho\mathbf{g}-\mathbf{S}_r(\mathbf{P}), \tag{2}$$

$$\frac{\partial E}{\partial t}+\nabla\cdot(E\mathbf{v}+\mathsf{P}\cdot\mathbf{v})=\rho\mathbf{g}\cdot\mathbf{v}-cS_r(E), \tag{3}$$

$$\frac{\partial E_r}{\partial t}+\nabla\cdot\mathbf{F}_r=cS_r(E), \tag{4}$$

$$\frac{1}{c^2}\frac{\partial\mathbf{F}_r}{\partial t}+\nabla\cdot\mathsf{P}_r=\mathbf{S}_r(\mathbf{P}), \tag{5}$$

where ρ, $\mathbf{v}$, $\mathbf{g}$ are the gas density, fluid velocity and the gravitational acceleration, $\mathsf{P}=p\mathsf{I}$ is the pressure tensor, $p=\rho k_B T_g/\mu m_{\rm H}$ is the gas pressure, I is the identity matrix, and $E=p/(\gamma-1)+\rho v^2/2$ is the total fluid energy density.

The radiation momentum and energy source terms $\mathbf{S}_r(\mathbf{P})$ and $S_r(E)$ are given by (Lowrie et al. 1999)

$$\begin{aligned}\mathbf{S}_r(\mathbf{P})=&-\frac{\sigma_F}{c}\left[\mathbf{F}_r-(\mathbf{v}E_r+\mathbf{v}\cdot\mathsf{P}_r)\right]\\&+\frac{\mathbf{v}}{c}(\sigma_{\rm P}a_rT^4-\sigma_E E_r),\end{aligned} \tag{6}$$

$$\begin{aligned}S_r(E)=&(\sigma_{\rm P}a_rT^4-\sigma_E E_r)\\&+\sigma_F\frac{\mathbf{v}}{c^2}\cdot\left[\mathbf{F}_r-(\mathbf{v}E_r+\mathbf{v}\cdot\mathsf{P}_r)\right],\end{aligned} \tag{7}$$

where E_r and $\mathbf{F}_r$ are the radiation energy density and radiation flux, T is the gas temperature, and σ_F, $\sigma_{\rm P}$ and σ_E are the flux mean opacity, the Planck mean opacity and the energy mean opacity correspondingly. The thermal and dynamical behaviors of dust and gas has been discussed in KT13 (see their Appendix A). In the parameter space we are concerned with, the dust is in thermal equilibrium with the radiation field, thus we have the dust temperature $T_{\rm dust}\simeq(E_r/a_r)^{1/4}$. On the other hand, the dust thermally couples with the gas only if the gas density exceeds $\sim 10^4-10^5$ cm^{-3} (e.g., Goldsmith 2001). As the ISM material is accelerated and spreads out, the gas no longer has the same temperature as the dust. However, since gas is highly supersonic in the outflow, the thermal pressure is much weaker compared to ram pressure, changing the gas temperature does not obviously affect the dynamics of the gas. For simplification we still assume $T_{\rm gas}=T_{\rm dust}=T$ in our work.

The radiation pressure P_r is given by $\mathsf{P}_r=\mathsf{f}E_r$, where f is the eponymous VET, which is calculate directly by

$$\mathsf{f}=\frac{\mathsf{P}_r}{E_r}=\frac{\int I(\hat{n})\mu_i\mu_j d\Omega}{\int I(\hat{n})d\Omega}, \tag{8}$$

where $d\Omega$ is the differential of solid angle, and $\mu_i\equiv\hat{n}\cdot\hat{x}_i$ is the cosine factor. The specific intensity of the radiation field I can be solved by the radiation transfer equation

$$\hat{n}\cdot\nabla I=\sigma_F\left(\frac{a_rc}{4\pi}T^4-I\right). \tag{9}$$

This equation is solved using the short characteristics method, as descried in detail in Davis et al. (2012).

For simplicity, we use the Planck $\kappa_{\rm P}$ and Rosseland $\kappa_{\rm R}$ mean opacities (KT12, KT13, D14)

$$(\kappa_{\rm P}, \kappa_{\rm R}) = (10^{-1}, 10^{-3/2}) \left(\frac{T}{10\,{\rm K}}\right)^2 \ {\rm cm^2\ g^{-1}}. \quad (10)$$

Equation (10) gives an approximation with a dusty gas at $T \lesssim 150\,{\rm K}$ (Semenov et al. 2003). We set $\sigma_F = \rho\kappa_R$ in equations (6) and (7).

2.2. *Dimensionless Units*

As shown in KT12, the system with gravity is characterized by two dimensionless numbers, i.e., the dimensionless Eddington ratio

$$f_{{\rm E},*} = \frac{\kappa_{{\rm R},*} F_*}{gc}, \quad (11)$$

and the optical depth

$$\tau_* = \Sigma \kappa_{{\rm R},*}. \quad (12)$$

Here we take $\kappa_{{\rm R},*} = \kappa_{\rm R}(\rho_*, T_*)$, where

$$T_* = \left(\frac{F_*}{a_r c}\right)^{1/4} \quad (13)$$

is the characteristic temperature. Physically, the atmosphere of a rapidly star-forming galaxy is initially set to have a temperature of T_* everywhere, $f_{{\rm E},*}$ and τ_* are the initial Eddington and optical depth of the atmosphere.

The characteristic sound speed are defines by

$$c_{s,*}^2 = \frac{k_{\rm B} T_*}{\mu m_{\rm H}}. \quad (14)$$

The scale height h_*, density ρ_* and time t_* are

$$h_* = \frac{c_{s,*}^2}{g}, \qquad \rho_* = \frac{\Sigma}{h_*}, \qquad t_* = \frac{h_*}{c_{s,*}}. \quad (15)$$

Following KT12 and D14, we choose $T_* = 82\,{\rm K}$, which corresponds to $F_* = 2.54 \times 10^{13}\, L_\odot\,{\rm kpc^{-2}}$, and $\kappa_{{\rm R},*} = 2.13\ {\rm cm^2\ g^{-1}}$.

The VET and Monte Carlo methods imply that a wind can be also launched for an initially sub-Eddington system with $f_{{\rm E},*} < 1$, while the FLD and M1 closure methods imply that a dusty wind can be launched only for $f_{{\rm E},*} > 1$. Nevertheless, if a dusty wind has been launched by radiation pressure or other mechanisms, it has already overcome its gravitational potential at the base of the system. Following KT13, we focus on the limit of $g \to 0$, i.e., $f_{{\rm E},*} \to \infty$ in our simulations. In this case an accelerating wind without gravity gives an upper limit of momentum transfer between radiation and dusty gas.

Next, we need to define another set of natural units for the gravity-free system. We use a characteristic acceleration

$$g_a = \frac{\kappa_{{\rm R},*} F_0}{c}, \quad (16)$$

which measures the radiation force on the dust. The units of length, time and density are defined using g_a instead of g:

$$h_a = \frac{c_{s,*}^2}{g_a} = \frac{h_*}{f_{{\rm E},*}} \qquad t_a = \frac{h_a}{c_{s,*}} = \frac{t_*}{f_{{\rm E},*}}$$
$$\rho_a = \frac{\Sigma}{h_a} = f_{{\rm E},*}\rho_*. \quad (17)$$

Note that the definitions of h_a, t_a and ρ_a are different from KT13. In KT13, h_a, t_a and ρ_a are functions of τ_*, but we set these variables to be independent on τ_*, which provides a common time and length scales since we consider only one value of $f_{E,*}$.

Simulation Parameters

Run	IC	$[L_x \times L_y]/h_a$	$N_x \times N_y$	$\Delta x/h_a$
T3H	T3_F0.5	256×4096	1024×16384	0.25
T10	T10_F0.5	256×4096	1024×16384	0.25
T1	T1_F0.5L	256×8192	500×16000	0.512
T3L	T3_F0.5L	256×8192	500×16000	0.512

Table 1
The initial conditions (IC) show the corresponding runs with gravity in D14. $L_x \times L_y$ is the size of the computational box in unit of h_a. $N_x \times N_y$ is the zones in the box. $\Delta x/h_a = 0.25$ for the high resolution, and $\Delta x/h_a = 0.512$ for the low resolution.

2.3. *Initial Conditions*

Since the gravitational field is set as $g = 0$ ($f_{{\rm E},*} \to \infty$), the simulation results only depends on τ_*. In this paper, we run four 2-dimensional simulations in the (x, y) plane with three values of τ_*. Two types of boundary conditions – hydrodynamic boundary and radiation boundary are set up for all simulations. Periodic boundary conditions are imposed in the horizontal direction ($x-$direction) on both the radiation and hydrodynamic variables. Reflecting and outflow boundary conditions are used on hydrodynamic variables at the bottom and the top of the vertical direction ($y-$direction) respectively, and inflow and vacuum boundary conditions are setup at the bottom and the top respectively.

Tables 1 summarizes simulation parameters for our runs. T3H and T3L correspond to $\tau_* = 3$, T10 correspond to $\tau_* = 10$, and T1 corresponds to $\tau_* = 1$. We run T3H and T10 with a high resolution $\Delta x/h_a = 0.25$, and T1 and T3L with a low resolution $\Delta x/h_a = 0.512$. In D14 (see also Rosdah & Teyssier 2015 and Tsang & Milosavljević 2015), the isothermal dusty atmosphere is initialized with initial density perturbation, which seeds the growth of RTI and turbulence. It is reasonable to assume that a wind launched at the base of a galaxy have already been in a fully turbulent state with small-scale structures. The initial conditions for gas-wind interaction in KT13 are setup by the end states of the simulations from KT12. Similarly, in this paper we choose the initial conditions from the end states in D14.

D14 considered various runs with a range of τ_* and $f_{{\rm E},*}$ with gravity. In particular, we focus on three runs: T10_F0.5 ($\tau_* = 10$, $f_{{\rm E},*} = 0.5$), T3_F0.5 ($\tau_* = 3$, $f_{{\rm E},*} = 0.5$), and T1_F0.5 ($\tau_* = 1$, $f_{{\rm E},*} = 0.5$) in D14. The size of the box for three runs are $[L_x \times L_y]/h_* = 512 \times 1024$, with a resolution of $L_{(x,y)}/N_{(x,y)} = 0.5 h_*$. We take the simulations results from T3_F0.5 and T10_F0.5. The gas in the atmosphere is accelerated by radiation, and eventually reach the top of the box as unbound outflow.

The gas in T3_F0.5 is accelerated to $\sim 1024h_*$ at $t \sim 80t_*$, and turbulence is well developed within the gas. We take the gas at $t = 80t_*$ as the initial state for run T3H. On the other hand, the gas in T10_F0.5 reaches the top of the box much earlier than that in T3_F0.5 due to a higher optical depth and a larger radiation force on the gas. We take the gas at $t = 37.5t_*$ as the initial state for run T10. Note that the resolution for T3H and T10 are the same as T3_F0.5 and T10_F0.5. We simply switch the scale h_* with gravity to h_a in this paper.

On the other hand, we run two simulations T1_F0.5L and T3_F0.5L, which have the same setup as T1_F0.5 and T3_F0.5 in D14 respectively, but using a lower resolution $L_{(x,y)}/N_{(x,y)} = 1.024h_*$. Different from other cases with $\tau_* > 1$, in T1_F0.5 the gas is only accelerated to a maximum height of $\sim 200h_*$ at $t \sim 80t_*$, then falls back to the base of the system, and eventually reaches a quasi-steady state at $t \sim 125t_*$. We take the gas at $t = 80t_*$ when the gas reaches its maximum height as the initial state for T1. T3_F0.5L gives a very similar result as T3_F0.5 in D14, but a slightly slower acceleration by radiation because of the lower resolution (see D14 for more discussion on the effects of spatial resolution). We choose the initial state of T3L at $t = 90t_*$ from T3_F0.5L. Note that T1 and T3L have the same resolution as T1_F0.5L and T3_F0.5L.

In all simulations, we expand the vertical direction of the domain box and initialize zones which are beyond the simulation domains in D14 by giving a uniform temperature $T_* = 82\,\mathrm{K}$, and $\rho = 10^{-10}\rho_*$ as the background. Low resolution runs (T1 and T3LR) were carried out on the *Rivanna* cluster at the University of Virginia, and high resolution runs (T3HR and T10) were carried out on the TACC cluster Stampede.

3. RESULTS

3.1. *Wind Properties*

We first consider the T3H run. Figure 1 shows five snapshots of the density field from this run. Without the gravitational confinement, the gas moves upward and expands in the vertical direction, with the initial filamentary structure is smoothed out in the radiation field. At $t \sim 59t_a$, the dense gas hits the upper boundary of the domain, and the gas expands to a thickness of $\sim 1300h_a$, which covers $\sim 35\%$ of the box. Most of the gas is in a few filaments with $\rho \sim 10^{-3} - 10^{-2}\rho_*$, in between the filaments the volume is filled with a gas of $\rho \gtrsim 10^{-5}\rho_*$. This result is different from KT13 (their Figure 2), in which more extended filamentary structure is driven by radiative RTI, and the vertical extent of the gas eventually becomes comparable to the vertical size of the entire computational box.

Figure 2 shows density snapshots for the run T10. Due to a higher initial optical depth, the gas is accelerated faster than that in T3. Although the initial turbulence is also smoothed out by radiation, the gas is more turbulent with larger velocity dispersion that the gas in T3. Between the filaments of dense gas, the volume has lower density $\rho \lesssim 10^{-6}\rho_*$. After $t = 30\,t_a$, the relative velocities at some shock fronts in the T10 run become very high (Mach numbers of $\lesssim 100$). In regions where shock fronts cross obliquely, the temperature spikes in low density zones adjacent to the shock front. The algorithm

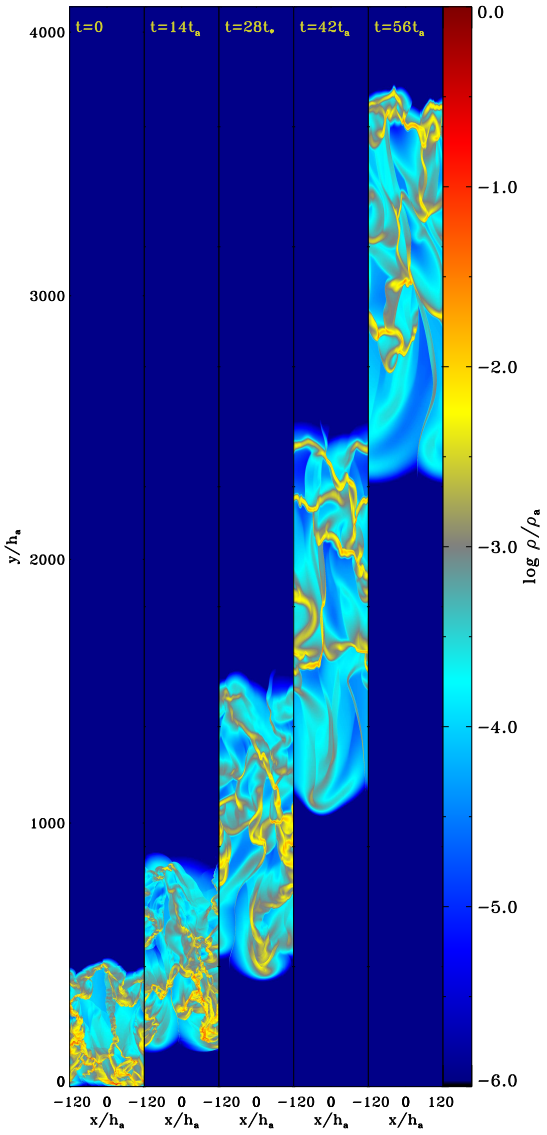

Figure 1. Density distribution ρ for five snapshots from run T3H.

compensates on the following timesteps by generating a large radiation flux that then artificially heats neighboring optically thick zones. From this point on energy is conserved only at the few percent level. By itself, this modest violation of energy conservation might not be troubling, but this uncontrolled heating produces artificially elevated temperatures at interfaces between low density channels and high density filaments. Due to the T^2 temperature dependence of the opacity, the radiation forces on the edges of the low density channels causes them to expand, creating voids that are not seen in other simulations or at earlier times in this simulation. Reducing the timestep reduces the temperature jumps, altering subsequent evolution. However, running with a significantly lower timestep would be prohibitively computationally expensive so we halt this run at $t = 30\,t_a$.

Figure 3 shows gas acceleration for $\tau_* = 1$. Simula-

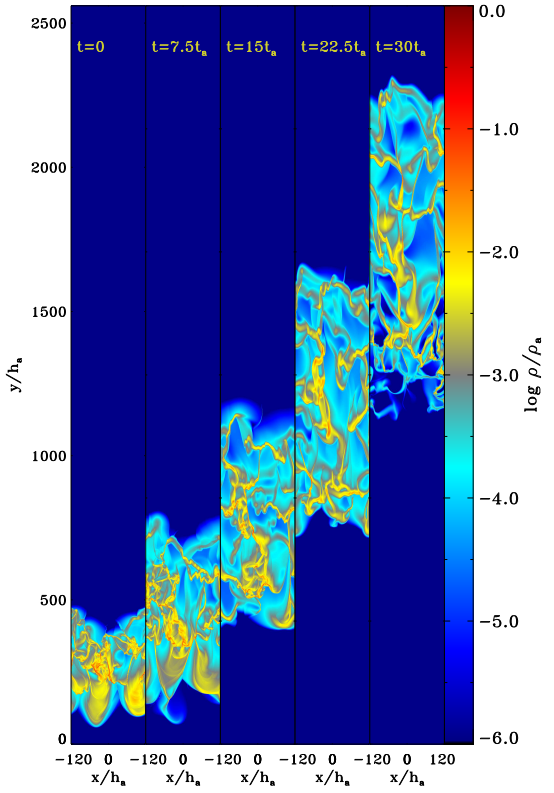

Figure 2. Density distribution ρ for five snapshots from run T10.

tions in D14 shows that gas in a gravitational field with $\tau_* \leq 1$ and $f_{E,*} \leq 0.5$ should fall back to the bottom of the system and maintains a quasi-steady state. In the absence of gravity the gas becomes unbound, and we study the behavior of the unbound gas. It reaches the top of the box at $t \sim 68t_a$ and spreads over a vertical height of $\sim 500h_a$, smaller and with lower velocity dispersion than the gas in T3 and T10.

Gas acceleration with various optical depths can be clearly seen in the mass-weighted mean velocity, which is given by

$$\langle \mathbf{v} \rangle = \frac{1}{M} \int \rho \mathbf{v} dV, \tag{18}$$

and mass-weighted velocity dispersion

$$\sigma_i^2 = \frac{1}{M} \int \rho (v_i - \langle v_i \rangle)^2 dV, \tag{19}$$

respectively, where $M = \int \rho dV$ is the total mass in the atmosphere. The left panel of Figure 4 shows the mean velocity in y direction $\langle \mathbf{v}_y \rangle$, and the total velocity $\sigma = \sqrt{\sigma_x^2 + \sigma_y^2}$ for T1, T3H and T10 runs. For convenience, we convert the dimensionless units in the simulations to cgs units. The velocity $\langle \mathbf{v}_y \rangle$ increases almost linearly with time. The timescale of gas acceleration to 50 km s^{-1} is ~ 100 kyr, which is comparable to the time to launch a wind from the base of the system. Gas with lower initial optical depth τ_* gives a slower acceleration. For example, $\langle \mathbf{v}_y \rangle$ reaches 50 km/s at $t \sim 150$ kyr in T1, but reaches the same velocity with a shorter time $t \sim 110$ kyr in T3H.

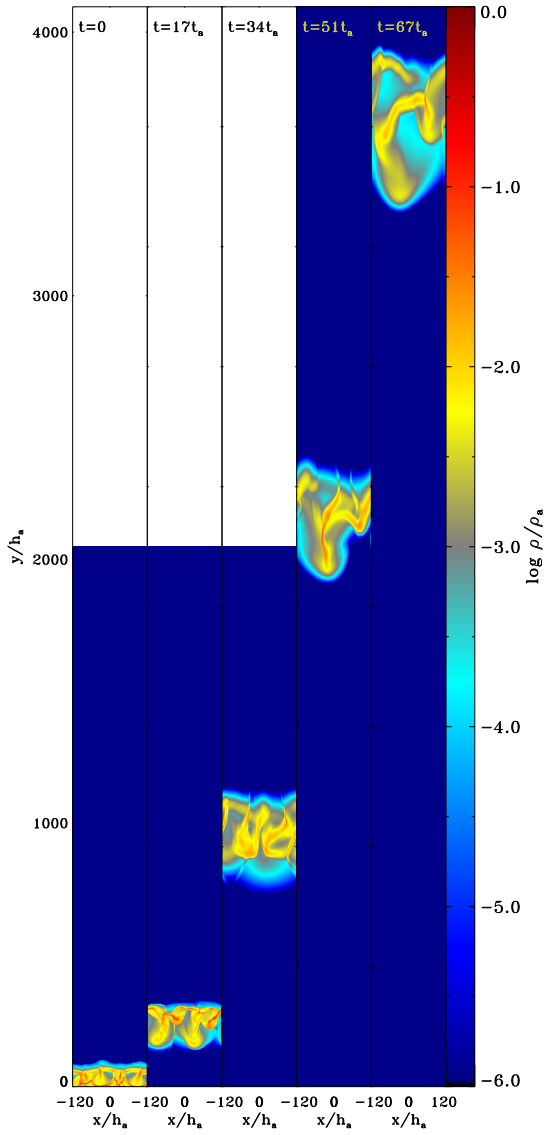

Figure 3. Density distribution ρ for five snapshots from run T1.

Also, lower τ_* leads to lower dispersion velocity. Velocity dispersion σ in T1 grows from ~ 2 km/s to 3.5 km/s at $t \sim 200$ kyr, while σ in T3H increases from 5 km/s to 7 km/s at $t \sim 80$ kyr, then oscillates at $\sim 6 - 7$ km/s at later time.

Note that the velocities obtained by radiation-pressure-acceleration in Figure 4 is far below the observed velocities of cold clouds, which can reach hundreds or even thousands of km s^{-1} (e.g., Heckman et al. 2000; Rupke et al. 2002, 2005a,b,c; Martin 2005; Weiner et al. 2009; Chen et al. 2010; Erb et al. 2012; Kornei et al. 2013). That is because in our simulations we only study wind propagation within a vertical height of $\sim 5 - 10$ pc. An estimate of the gas velocity on a larger scale is discussed in Section 4.

3.2. *Spatial Resolution*

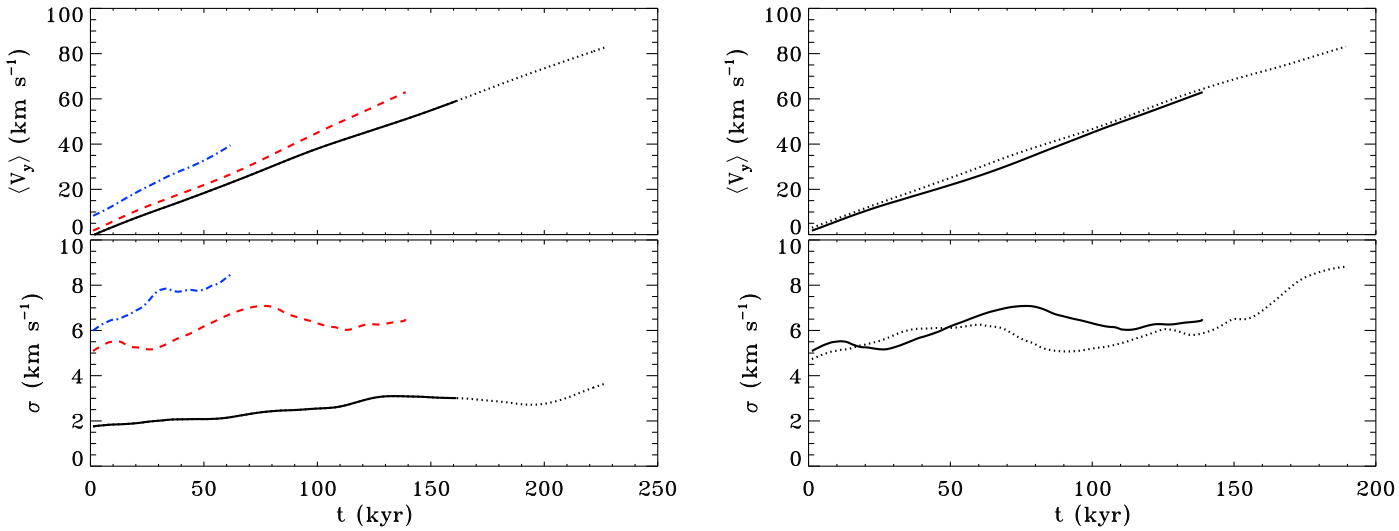

Figure 4. Left: mean gas velocity as a function of time for three runs T1 (black), T3H (red dash) and T10 (blue dash-dotted). The solid black shows the gas acceleration in T1 in a box with the same height ($4096h_a$) as in T3H and T10, the dotted black shows the gas acceleration in T1 to a height of $8192h_a$. Right: mean gas velocity as a function of time for T3H (solid) and T3L (dotted). The gas in T3L is accelerated to a height of $8192h_a$.

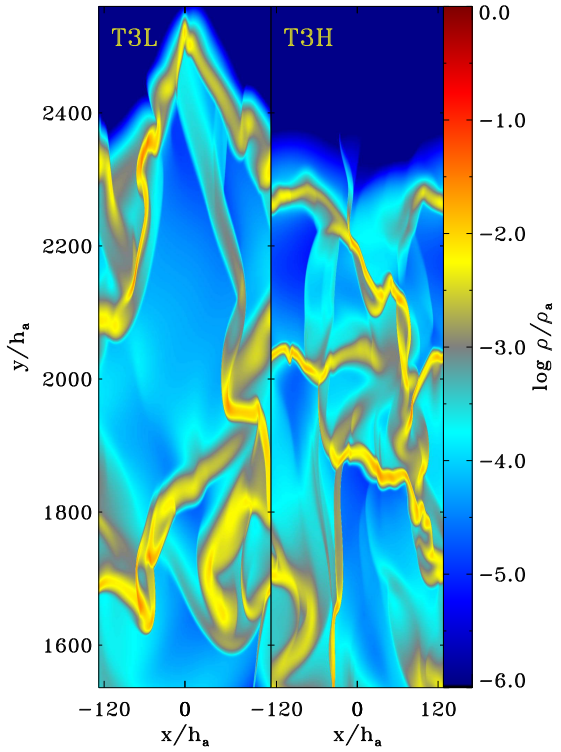

Figure 5. Comparison of density distribution ρ between T3L and T3H.

We have performed simulations with the same initial conditions $\tau_* = 3$, with a high resolution in the T3H run, and a low resolution in the T3L run. Since the low resolution run is less expensive, we run T3L a bit longer than T3H. We run T3L in a box with a vertical height of $8192h_a$, which is twice as that in the higher-resolution T3H. The right panel of Figure 4 compares $\langle \mathbf{v}_y \rangle$ and σ in T3H and T3L. Although the initial conditions from T3_F0.5 and T3_F0.5L are slightly different, the two runs with different initial inputs show very similar acceleration. The velocity dispersion σ increases more quickly in T3H at $t \lesssim 80$ kyr, but both σ become flat at $80\,\mathrm{kyr} \lesssim t \lesssim 140$ kyr, then σ in T3L slightly increases to $9\,\mathrm{km\ s^{-1}}$ by the end of the simulation.

Figure 5 shows the snapshots of the density distribution ρ from T3L and T3H at a same time $t = 40t_a$. The gas in T3L is accelerated more quickly than that in T3H. The front of the gas in T3L reaches a height of $h \sim 2600h_a$, when the gas in T3H only reaches $h \sim 2300h_a$. The structure at the top of the gas in two runs are different: T3L shows a more dense front head than the gas in T3H. In general, the gas in T3L is less structured, and less turbulent than the gas in T3H. The difference in structures is presumably due to the fact that T3L does not resolve h_*. Nevertheless, the similar acceleration in the two cases suggests resolving h_* might not be essential for obtaining the correct value for the bulk radiative acceleration of the outflow. This would bode well for larger scale simulations of radiative outflows where resolution of h_* would require prohibitively high resolution.

3.3. *Trapping Factor*

We study the momentum coupling between the infrared radiation field and the gas. Without gravity, the y-component momentum equation of the gas is

$$\frac{d\langle v_y \rangle}{dt} = f_{\rm rad}, \tag{20}$$

where $f_{\rm rad}$ is defined as the mean radiation force per unit mass

$$f_{\rm rad} = \frac{1}{c}\frac{\langle \kappa_{\rm R} \rho F_{ry} \rangle}{\langle \rho \rangle}. \tag{21}$$

Following KT13, we define the trapping factor $f_{\rm trap}$ in a gravity-free field by

$$1 + f_{\rm trap} = \frac{f_{\rm rad}}{f_{\rm rad,dir}} \tag{22}$$

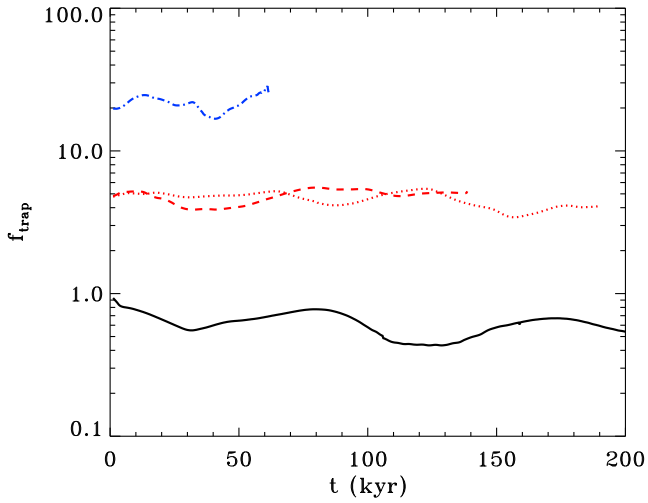

Figure 6. Trapping factors as a function of time for four runs: T1 (black solid), T3L (red dotted), T3H (red dashed) and T10 (blue dash-dotted).

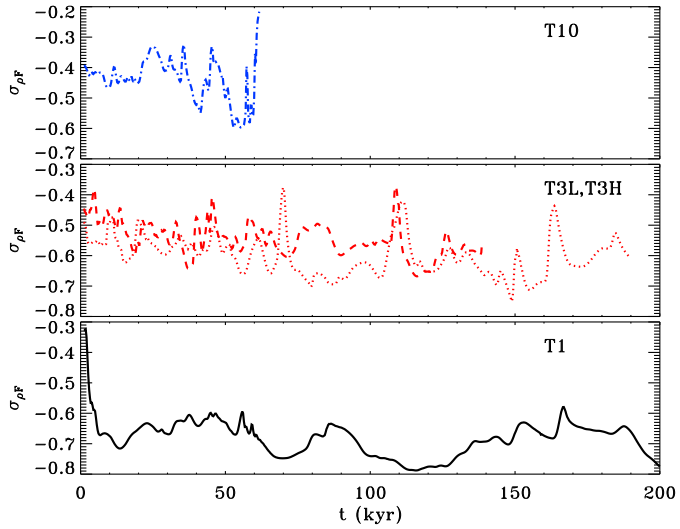

Figure 7. Correlation between density and flux weighted by density $\sigma_{\rho \mathrm{F}}$. The lines have the same meaning as in Figure 6.

where $f_{\mathrm{rad,dir}} = F_{ry}/(c\langle\rho\rangle L_y) = F_*/(c\langle\rho\rangle L_y)$ is the momentum flux per unit mass of the directly injected radiation field. Thus, equation (20) can be re-written as

$$f_{\mathrm{trap}} = \frac{t_a \tau_*}{c_{s,*}} \frac{d\langle v_y\rangle}{dt} - 1. \tag{23}$$

The trapping factor f_{trap} measures the momentum transfer from the radiation to the gas. The upper limit of trapping in analytic models adopts $f_{\mathrm{trap}} \sim \tau_{\mathrm{IR}}$, where τ_{IR} is the infrared optical depth of the system. In our simulations, the initial f^0_{trap} is obtained from the end state of the gas at the base of the system with gravity (KT12 and D14)

$$1 + f^0_{\mathrm{trap}} = L_y \frac{\langle \kappa_R \rho F_{ry}\rangle}{\langle F_{ry}\rangle} = \frac{f_{\mathrm{rad}}\tau_*}{g_* f_{E,*}} = \frac{\tau_* f_{E,V}}{f_{E,*}}, \tag{24}$$

where $f_{E,*}$ is computed before gravity is turned off ($f_{E,*} = 0.5$), and

$$f_{E,V} = \frac{f_{\mathrm{rad}}}{g_*} \tag{25}$$

is the Eddington ratio computed using the initial gravity g_*. According to KT12 and D14, $f_{E,V} \sim 1$ due to the radiative RTI regulation, therefore,

$$f^0_{\mathrm{trap}} \simeq \frac{\tau_*}{f_{E,*}} - 1. \tag{26}$$

We have $f^0_{\mathrm{trap}} \simeq 1$ for $\tau_* = 1$, $f^0_{\mathrm{trap}} \simeq 5$ for $\tau_* = 3$, and $f^0_{\mathrm{trap}} \simeq 19$ for $\tau_* = 10$.

KT13 found that f_{trap} without gravity significantly deceases from f^0_{trap} to a smaller value due to radiative RTI. Figure 6 shows trapping factor as a function of time in

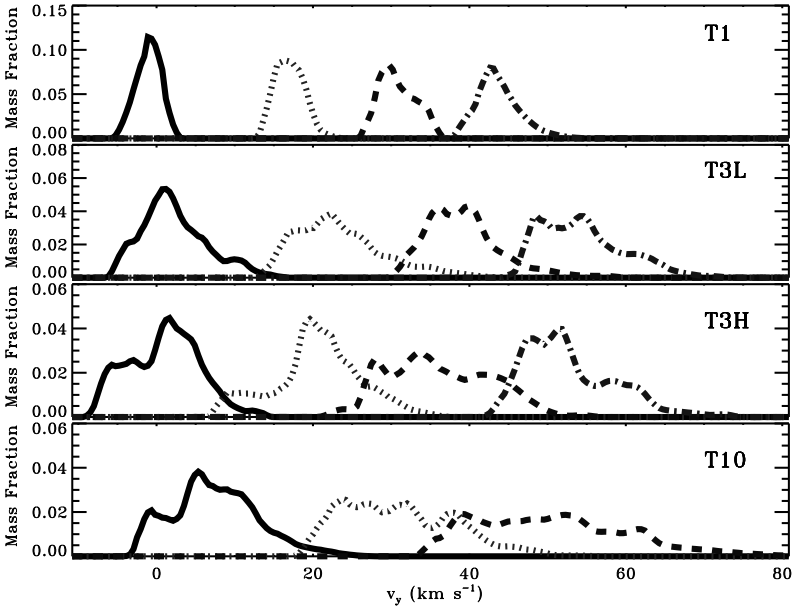

Figure 8. Velocity distribution functions for run T1, T3L, T3H and T10 at $t/t_a = 0$ (solid), 15 (dotted), 30 (dashed) and 45 (dash-dotted).

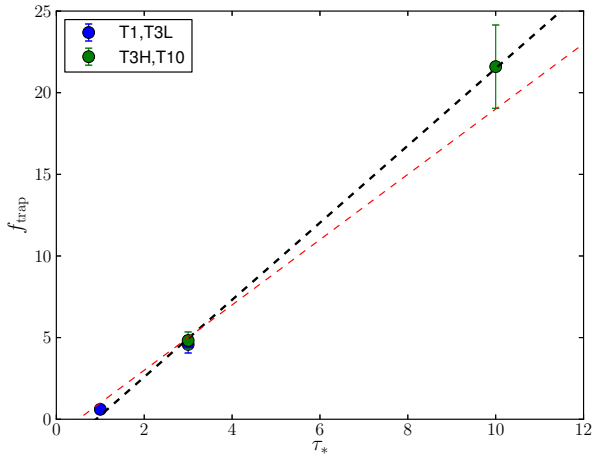

Figure 9. Trapping factors as a function of time time for four runs. The black dashed line is the linear fitting of the points, and red dashed line is $f_{\rm trap} = \tau_*/(f_{E,*})_0 - 1$.

our simulations. In contrast, we do not see any significant evolution of the trapping factor. Comparison of $f_{\rm trap}$ for T3L and T3H suggests that the trapping property is insensitive to the resolution. The values of $f_{\rm trap}$ are largely consistent with the values $f^0_{\rm trap}$ inferred from the D14 runs with gravity. Thus, it is perhaps somewhat surprising that the runs performed here with $g = 0$ see little evolution of the trapping factor. One possibility is that RTI has much less affect on trapping factor in these runs with $g = 0$ and the simulations simply retain knowledge of their initial density and flux distributions. Since the RTI largely shapes the trapping factor through its effect on the flux – density relationship, we calculate the density-weighted correlation between density ρ and the vertical component of radiation flux F_{ry}

$$\sigma_{\rho F} = \frac{\langle \rho(\rho - \langle\rho\rangle)(F_{ry} - \langle F_{ry}\rangle)\rangle}{\sqrt{\langle \rho(\rho - \langle\rho\rangle)^2\rangle}\sqrt{\langle \rho(F_{ry} - \langle F_{ry}\rangle)^2\rangle}}. \quad (27)$$

We average $\sigma_{\rho F}$ over the entire domain and plot it in Figure 7. Since density and flux are anti-correlated, we find a negative value for $\sigma_{\rho F}$, with lots of short timescale fluctuation but no long term evolution.

These results suggest that the RTI has relatively little impact on the long term evolution of the flux–density correlation in our simulations. Note that different from other three runs, the correlation $\sigma_{\rho F}$ in T1 drops quickly from $\sigma_{\rho F} \sim -0.3$ to $\sigma_{\rho F} \sim -0.7 - -0.6$, that is because the system transits from a quasi-steady state in gravity to an unbound state without gravity. Over the course of this run, $f_{\rm trap}$ also drops within a factor of two, which is larger than other three runs. However, we still find that $f_{\rm trap} \sim f^0_{\rm trap}$ in all the runs, which can be interpreted simply as the solution preserving its initial condition. It is less clear why VET and FLD methods find different results. Comparison of our results with KT13 shows that their simulations form long, vertically oriented low-density channels where flux can escape, while our simulations do not. The analysis from D14 suggests that FLD acts to more strongly reinforce the development of non-linear structure and this same tendency may be at play here. Analysis of the linear instability to radiative RTI (Jacquet & Krumholz 2011) in optically thin and adiabatic limits suggests these flows should be linearly stable when $g \to 0$. This does not preclude non-linear interactions that cause channels to develop or widen, but neither is there a clear motivation for radiative RTI to continue to shape the density structure in a manner that would have strong impact on the momentum coupling between gas and radiation.

3.4. *Velocity Distribution*

Figure 8 shows mass-weighted velocity probability distribution functions (PDFs) in y-direction for four runs: T1, T3L, T3H and T10. Since the initial condition for T1 is quasi-steady, the velocity distribution is nearly symmetric at $v_y = 0$. On the other hand, the initial velocity distributions for T3L, T3H and T10 are asymmetric with a tail extending to $v_y \sim 20 - 30$ km s^{-1}, indicating that most of the gas has already been accelerated at the base of the system. As time evolves, the PDFs for all runs shift to higher velocity of v_y. Higher τ_* gives a higher acceleration, and a larger spreading of velocities. This is consistent with Figure 4 that larger τ_* leads to faster acceleration and larger velocity dispersion. Also,the panels for T3L and T3H show that resolution does not change the PDF qualitatively.

4. DISCUSSION

4.1. *Momentum Transfer Between Radiation and Gas*

In KT13, a linear fit of $f_{\rm trap}$ is given by $f_{\rm trap} \approx 0.5$ in the limit of $f_{E,*} \to \infty$. They adopt an interpolation for $f_{\rm trap}$ as a function of τ_* and $f_{E,*}$, and conclude that winds can only be produced from systems with $f_{E,*} \gtrsim 1$ (super-Eddington limit). However, using the VET method we find different conclusions. In this section we put gravity back to estimate wind acceleration by radiation in a gravity field.

Note that Figure 6 shows that $f_{\rm trap}$ is approximately flat without gravity $f_{E,*}$. Recall the relation that

$$f_{E,V} = (1 + f_{\rm trap}) \frac{f_{E,*}}{\tau_*}. \tag{28}$$

For $f_{E,*} < 1$, the radiative RTI regulates equilibrium between infrared radiation and gravity. Thus, we have $f_{E,V} \sim 1$, and $f_{\rm trap} \simeq \tau_*/f_{E,*} - 1$. On the other hand, Figure 9 shows values of $f_{\rm trap}$ as a function of τ_* in the limit of $f_{E,*} \to \infty$. We find that the estimate $f_{\rm trap} \sim f^0_{\rm trap} \simeq \tau_*/(f_{E,*})_0 - 1$ holds, where $(f_{E,*})_0$ is the initial Eddington ratio where the wind is launched. Figure 9 is consistent with Figure 6.

Including gravity, equation (20) can be written as

$$\frac{d\langle v_y \rangle}{dt} = f_{\rm rad} - g, \tag{29}$$

or

$$\begin{aligned} \frac{dp_{\rm wind}}{dt} &= (1 + f_{\rm trap}) \left(1 - \frac{1}{f_{E,V}}\right) \frac{L}{c} \\ &\approx (f_{E,V})_0 \frac{\tau_*}{(f_{E,*})_0} \left[1 - \frac{(f_{E,*})_0}{f_{E,*}} \frac{1}{(f_{E,V})_0}\right] \frac{L}{c} \end{aligned} \tag{30}$$

Here $dp_{\rm wind}/dt$ is the momentum injection as a combination of both infrared radiation acceleration and gravitational deceleration. Note that $f_{E,V}/f_{E,*} \sim (f_{E,V})_0/(f_{E,*})_0$, or $f_{E,V} \simeq f_{E,*}(f_{E,V})_0/(f_{E,*})_0$ according to our simulations. Since $(f_{E,V})_0 \sim 1$, we obtain

$$\frac{dp_{\rm wind}}{dt} \simeq \frac{\tau_*}{(f_{E,*})_0} \left[1 - \frac{(f_{E,*})_0}{f_{E,*}}\right] \frac{L}{c}, \tag{31}$$

For a infrared optical thick disk, the gravitational force drops faster than the radiation force with the height, $f_{E,*}$ increases monotonically, the Eddington ratio above the disk is higher than that at the base of the system, i.e. $f_{E,*} > (f_{E,*})_0$ (e.g., Zhang & Thompson 2012). If we include the direct radiation from the stellar UV light, we have the total momentum injection from radiation

$$\frac{dp_{\rm wind}}{dt} \sim \left[1 + \frac{\tau_*}{(f_{E,*})_0}\right] \frac{L}{c}, \tag{32}$$

This is consistent with the result obtained at the base of the system (see Section 5.4 in D14). According to D14, $\tau_*/(f_{E,*})_0$ represents the effective infrared optical depth for momentum transfer, which is slightly lower that $\tau_{\rm IR}$ of the system. Here $\tau_{\rm IR}$ can be estimated by the volume-weighted mean optical depth

$$\tau_V = L_y \langle \kappa_R \rho \rangle. \tag{33}$$

We average τ_V in our simulations and find $\langle \tau_V \rangle = 1.8$ in T1, 7.9 in T3L, 8.5 in T3H and 48.3 in T10, thus, we can define the efficiency η where $\eta\tau_{\rm IR}$ is equivalent to $\tau_*/(f_{E,*})_0$. Thus, we find $\eta = 0.90$ in T1, 0.71 in T3L, 0.69 in T3H, and 0.47 in T10. Therefore, we conclude that for $f_{E,*} > (f_{E,*})_0$, radiation pressure on dust is able to drive an unbound wind. The momentum transfer from the radiation field to the gas is amplified by a factor of $\eta\tau_{\rm IR}$ with $\eta \sim 0.5 - 0.9$, increasing with the optical depth in the atmosphere.

On the other hand, if $f_{E,*} < (f_{E,*})_0$, the wind may eventually fall back and be bound.

4.2. *Rapidly Star-Forming Galaxies and Starbursts*

Since τ_* and $f_{E,*}$ are the most important parameters in the simulations, it is worthwhile to estimate them in real rapidly star-forming galaxies and starbursts. KT13 calculated τ_* and $f_{E,*}$ analytically using a mass-to-light ratio motivated by the starburst99 model (Leitherer 1999). We estimate τ_* and $f_{E,*}$ using recent observation data. We consider the gas surface density in a galactic disk is $\Sigma_{\rm g} = 10^4 \Sigma_{\rm g,4}\, M_\odot$ pc^{-2}, the infrared flux is $F_{\rm IR} = 10^{13} F_{\rm IR,13}\, L_\odot$ kpc^{-2}, where $10^4\, M_\odot$ pc^{-2} (2.1 g cm^{-2}), and $10^{13}\, L_\odot$ kpc^{-2} are the typical surface densities and fluxes in LIRGs/ULIRGs (e.g., Thompson et al. 2005). The characteristic temperature in the atmosphere is given by $T_* = (F_{\rm IR}/a_r c)^{1/4}$, and the surface gravitational force is $g = 2\pi G \Sigma_{\rm g} f_g^{-1}$, where $f_g = 0.5 f_{g,0.5}$ is the mass fraction of the gas. Thus, we have

$$\tau_*^{\rm max} = 2.8\, \Sigma_{\rm g,4} F_{\rm IR,13}^{1/2}, \tag{34}$$

$$f_{E,*} = 0.10 f_{\rm g,0.5} F_{\rm IR,13}^{3/2} (\Sigma_{\rm g,4})^{-1}. \tag{35}$$

Here, equation (34) gives an upper bound of the infrared optical depth in the atmosphere of the galaxy. We estimate these two values using the most recent observation of LIRGs and ULIRGs measured and compiled by Barcos-Muñoz et al. (2016, submitted). They have observed 22 local LIRGs and ULIRGs using the Very Large Array radio observation. We take LIRGS/ULRIGs in their work as a sample. Since molecular gas is presumably the dominant component in LIRGs and ULIRGs, especially in the central regions, we use their molecular gas density $\Sigma_{\rm mol}$ as our estiamte for Σ_g[1].

[1] Note that the measurements of $\Sigma_{\rm mol}$ are uncertain, depending on the assumed conversion factor of CO to H_2, and the assumption that the emitting area is well-charaterized by the 33 GHz emission.

Using the data in Barcos-Muñoz et al. (2016), we find that most LIRGs/ULIRGs have $f_{E,*} < 1$, and about one fourth of them have $f_{E,*} \sim 0.1-1$. The values of $\tau_*^{\rm max}$ are typically large $\tau_*^{\rm max} \gtrsim 1-10$, suggesting a large $\tau_* \gtrsim 1$ in the atmosphere is possible. For example, Arp 220 has molecular gas density $\Sigma_{\rm mol} \sim 4.9\times10^4\,M_\odot$ pc^{-2} and a flux of $F_{\rm IR} \sim 6.1\times10^{13}\,L_\odot$ kpc^{-2}, corresponding to $f_{E,*} \sim 0.3$ and $\tau_*^{\rm max} \sim 30$. Although τ_* of the atmosphere is much less the total τ_*, we still expect $\tau_* \gtrsim 1$. Our simulation suggests that the infrared radiation may launch dusty gas out of the galaxy, as $f_{E,*}$ drops above the galactic disk, the gas may be accelerated and become unbound. Moreover, an extreme case is given by the ULRIG Mrk 231 (UGC 08058) with $\Sigma_{\rm mol} \sim 1.7\times10^5\,M_\odot$ pc^{-2} and $F_{\rm IR} \sim 2.6\times10^{14}\,L_\odot$ kpc^{-2}, corresponding to $f_{E,*} \sim 0.8$ and $\tau_*^{\rm max} \sim 2.3\times10^2$. Although Mrk 231 has active galactic nucleus activities (e.g., Rupke & Veilleux 2013), we expect that infrared radiation alone could drive a powerful dusty wind in Mrk 231.

In general, we find many of the systems in the Barcos-Munoz sample have $f_{E,*} < 1$ and $\tau_* > 1$. Since gas can be launched by radiation from an initially sub-Eddington system, and as $f_{E,*}$ increases with the height above the ULIRG disk, gas can potentially be accelerated to the observed velocities. Therefore, our results suggest that radiation pressure may still be an important mechanism to drive winds in a subset of observed rapidly star-forming galaxies and starbursts.

5. CONCLUSIONS

We study the dusty winds driven by radiation pressure in the atmosphere of rapidly star-forming environment. Krumholz & Thompson (2013) (KT13) used flux-limited diffusion algorithm to a two-dimensional problem modeling the radiation hydrodynamics (RHD) of a column of gas that is accelerated by a constant infrared radiation flux. We apply the more sophisticated variable Eddington tensor (VET) algorithm to re-examine the problem in KT13. In the absence of gravity, the system, which is characterized by the initial optical depth (τ_*) of the gas and the initial conditions, gives an upper limit on momentum transfer between radiation and gas. We carry out four runs with different τ_* and varying resolutions. In each simulation, the initial state of the gas is given by the end state of simulation in D14 with the same τ_* and resolution, but including gravity ($f_{E,*} = 0.5$). In D14 the gas evolves only at the base of the system. We expand the vertical direction of the computational domain, and study the wind-gas interaction and momentum coupling between the radiation field and the gas.

We find that the gas spreads out along the height of box with increased mean velocity and velocity dispersion, due to the interactive of the dusty gas and the radiation force. However, the radiative RTI does not seem to be limiting momentum transfer as in KT13. We find that the momentum coupling between gas and radiation in the absence of gravity is similar to that with gravity. The trapping factor $f_{\rm trap}$, which measures the momentum transfer from the radiation to the gas (see equations [22]), has the same value to within a factor of two or less at the base of the system. Combing the results in D14, we conclude that dusty gas can be accelerated by radiation even in an initially sub-Eddington system $f_{E,*} < 1$, and the momentum from the radiation couples well with the gas during the wind propagation. For $f_{E,*}$ increasing along the height of the system, the momentum transfer from radiation to gas is approximate

$$\frac{dp_{\rm wind}}{dt} \simeq \left\{1+\eta\tau_{\rm IR}\left[1-\frac{(f_{E,*})_0}{f_{E,*}}\right]\right\}\frac{L}{c}, \qquad (36)$$

where $(f_{E,*})_0$ is the Eddington ratio at the base of the system, $\tau_{\rm IR}$ is the integrated infrared optical depth through the dusty gas, and the efficiency η is estimate to be $\sim 0.5-0.9$ from $\tau_* = 1$ to $\tau_* = 10$. Thus, the momentum transfer from the radiation to the wind is not merely $\sim L/c$, but is amplified by a factor of $\eta\tau_{\rm IR}$. Therefore, we conclude that radiation pressure may still be a important mechanism to drive winds in rapidly star-forming galaxies and starbursts.

More discussion on these assumptions is given in Barcos-Muñoz et al. (2016).

We thank Yan-Fei Jiang and James Stone for stimulating discussions and comments. We are also grateful to Norman Murray for helpful discussion. D. Z. also thanks Todd Thompson, Mark Krumholz, Evan Scannapieco, Chris Hayward, Nahum Arav, Mike McCourt, Eliot Quataert, Eve Ostriker, Renyue Cen, Mordecai-Mark Mac Low, Greg Bryan, Kohei Inayoshi, Yong Zheng, Zhi-Yun Li, Alberto Bolatto, Sylvain Veilleux, Francesco Tombesi, Karen Yang, and Loreto Barcos-Muñoz for helpful discussions. This work used the Extreme Science and Engineering Discovery Environment (XSEDE), which is supported by National Science Foundation (NSF) grant No. ACI-1053575. This work also used the computational resources provided by the Advanced Research Computing Services (ARCS) at the University of Virginia. S. W. D. acknowledges support from NSF grant AST-1616171 "The Physics of Star Formation Feedback and Molecular Cloud Destruction" and an Alfred P. Sloan Research Fellowship.

REFERENCES

Andrews, B. H., & Thompson, T. A. 2011, ApJ, 727, 97
Chen, Y.-M. et al. 2010, AJ, 140, 445
Davis, S. W., Stone, J. M., & Jiang, Y.-F. 2012, ApJS, 199, 9
Davis, S. W., Jiang, Y.-F., Stone, J. M., & Murray, Norman 2014, ApJ, 796, 107 (D14)
Erb, D. K., Quider, A. M., Henry, A. L., & Martin, C. L. 2012, ApJ, 759, 26
Goldsmith P. F., 2001, ApJ, 557, 736
Heckman, T., Lehnert, M. D., Strickland D. K., & Lee, A. 2000, ApJS, 129, 493
Hopkins, P. F., Quataert, E., & Murray, N. 2011, MNRAS, 417, 950
Hopkins, P. F., Kereš, D., Murray, N., Quataert, E., & Hernquist, L. 2012, MNRAS, 427, 968
Hopkins, P. F., Quataert, E., & Murray, N. 2012, MNRAS, 421, 3488
Hopkins, P. F., Quataert, E., & Murray, N. 2012, MNRAS, 421, 3522
Jacquet, E., & Krumholz, M. R. 2011, ApJ, 730, 116
Jiang, Y.-F., Stone, J. M., Davis, S. W. 2012, ApJS, 199, 14
Kornei, K. A., Shapley, A. E., Martin, C. L., Coil, A. L., Lotz, J. M., & Weiner, B. J. 2013, ApJ, 774, 50
Krumholz, M. R., Klein R. I., McKee, C. F., & Bolstad, J. 2007, ApJ, 667, 626
Krumholz, M. R., & Matzner, C. D. 2009, ApJ, 703, 1352

Krumholz, M. R., & Thompson, T. A. 2012, ApJ, 760, 155 (KT12)
Krumholz, M. R., & Thompson, T. A. 2013, MNRAS, 434, 2329 (KT13)
Leitherer C. et al., 1999, ApJS, 123, 3
Lowrie, R. B., Morel, J. E., & Hittinger, J. A. 1999, ApJ, 521, 432
Martin, C. L. 2005, ApJ, 621, 227
Murray, N., Quataert, E., & Thompson, T. A. 2005, ApJ, 618, 569
Murray, N.; Quataert, E., & Thompson, T. A. 2010, ApJ, 709, 191
Murray, N., Ménard, B., & Thompson, T. A. 2011, ApJ, 735, 66
Oppenheimer, B. D., & Davé, R. 2006, MNRAS, 373, 1265
Oppenheimer, B. D., & Davé, R. 2008, MNRAS, 387, 577
Rosdahl, J., & Teyssier, R. 2015, MNRAS, 449, 4380
Rupke, D. S., Veilleux, S., & Sanders, D. B. 2002, ApJ, 570, 588
Rupke, D. S., Veilleux, S., & Sanders, D. B. 2005, ApJS, 160, 87
Rupke, David S., Veilleux, S., & Sanders, D. B. 2005, ApJS, 160, 115
Rupke, D. S., Veilleux, S., & Sanders, D. B. 2005, AJ, 632, 751
Rupke, D. S. N., & Veilleux, S. 2011, ApJ, 729, 27L
Semenov, D., Henning, T., Helling, C., Ilgner, M., & Sedlmayr, E. 2003, A&A, 410, 611
Stone, J. M., Gardiner, T. A., Teuben, P., Hawley, J. F., Simon, J. B. 2008, ApJS, 178, 137
Thompson, T. A., Fabian, A. C., Quataert, E., & Murray, N. 2015, MNRAS, 449, 147
Thompson, T. A., Quataert, E., & Murray, N. 2005, ApJ, 630, 167
Tsang, Benny T.-H., & Milosavljević, M. 2015, MNRAS, 453, 1108
Weiner, B. J., et al. 2009, ApJ, 692, 187
Wise, J. H., Abel, T., Turk, M. J., Norman, M. L., & Smith, B. D. 2012, MNRAS, 427, 311
Zhang, D., & Thompson, T. A. 2012, MNRAS, 424, 1170